Defect chemistry to trigger zirconia densification at low temperatures by Spark Plasma Sintering

Etienne Martin, U-Chan Chung, Mathieu Duttine, Marie Anne Dourges, Guillaume Clermont, Christine Labrugère-Sarroste, Sébastien Fourcade, Dominique Michau, Claude Estournès, Thomas Hérisson de Beauvoir, et al.

Defect chemistry to trigger zirconia densification at low temperatures by Spark Plasma Sintering

E. Martin[1], U.C. Chung[1], M. Duttine[1], M.A. Dourges[2], G. Clermont[2], C. Labrugère[3], S. Fourcade[1], D. Michau[1], C. Estournès[4], T. Hérisson de Beauvoir[4], F. Mauvy[1], V. Jubera[1], M. Maglione[1], G. Goglio[1] and C. Elissalde[1*]

1. Univ. Bordeaux, CNRS, Bordeaux INP, ICMCB, UMR5026, F-33600 Pessac, France
2. Univ. Bordeaux, CNRS, ISM, UMR 5255, F-33400 Talence, France.
3. Univ. Bordeaux, PLACAMAT, UAR 3626, F-33600 Pessac, France
4. CIRIMAT, CNRS-INP-UPS, Université Toulouse 3 – Paul Sabatier, 118 route de Narbonne, 31062 Toulouse, France

*Corresponding author e-mail address: catherine.elissalde@icmcb.cnrs.fr

Abstract

In-depth control of reactivity and defects chemistry is shown to be mandatory to reach high density YSZ ceramics at sintering temperatures lower than 900°C. The combination of Cold Sintering Process (CSP) and Spark Plasma Sintering (SPS) has highlighted the role of transient chemistry on the densification of this material. More, optimised conditions were found for achieving densification of YSZ at 850°C in a one-step SPS process. In particular, the vacuum level in the SPS chamber is clearly shown to be a decisive parameter to obtain dense nanostructured YSZ tetragonal ceramics up to 95% below 900°C. The occurrence of oxygen vacancies has thus been addressed associating thermal analyses, X-ray photoelectron spectroscopy, Electron Paramagnetic Resonance, photoluminescence spectroscopy and impedance spectroscopy. Understanding defect chemistry mechanisms and their dependence on the process or combination of processes, is a lever towards high-quality YSZ nanostructured ceramics below 900°C.

Key words: yttria stabilized zirconia, Spark Plasma Sintering, defect chemistry, impedance spectroscopy

Introduction

The different structural polymorphs of zirconia based ceramics are widespread used in a large variety of applications, but they also bring issues with regard to their sintering and properties control. In particular, the tetragonal-monoclinic transformation has attracted a considerable attention due to its role in the toughening reinforcement [1]. Many studies have focused on the stabilization of the metastable tetragonal phase [2]. The use of undoped zirconia nanopowder with critical grain size below 30 nm

seems to lead to a metastable tetragonal phase [3]. A high content of surface defects, absorbed hydroxyls and oxygen vacancies, also impacts the stabilization of the tetragonal phase [4]. The prominent role of the content of oxygen vacancies and the associated structural disorder on the tetragonal and cubic phases stabilization, has been highlighted through experiments and simulations [5,6]. Moreover, to stabilize the tetragonal and/or the cubic phase in dense ceramics at room temperature, the efficiency of the doping strategy has been widely proven. The most common stabilizers are calcium oxide (CaO), magnesium oxide (MgO), cerium oxide (CeO_2) and yttrium oxide (Y_2O_3). Divalent Ca^{2+} and Mg^{2+} cations preferably stabilize the cubic phase [7]. To stabilize zirconia's tetragonal phase, a sevenfold coordination of zirconium cations is favourable. The oxygen density in the vicinity of zirconium may be reduced by a steric effect through lattice dilatation due to the eightfold coordination of the Ce^{4+} [8]. Conversely, the number of oxygens around the zirconium can be reduced by introducing oxygen vacancies as compensating centers when using Y^{3+} dopant [9]. Oxygen deficiencies in zirconia can thus be introduced by thermal, surface, steric or charge effects. Defect chemistry plays therefore an important role in zirconia structure adaptation, but its impact on densification mechanisms has been scarcely investigated. Focusing on yttria stabilized zirconia, significant gain on decreasing sintering temperature have been achieved thanks to unconventional process such as Spark Plasma Sintering (SPS) [10-12]. Nearly fully dense 3Y-ZrO_2 can be obtained in the temperature range 1050-1200°C depending on the soaking time and applied pressure. Recently, A. Flaureau *et al.* have obtained fully dense 3Y-ZrO_2 ceramics at only 1050°C using initial nanoparticles (<20nm) [13]. Fairly good agreement on the densification mechanism is proposed for SPS performed at moderate stress/medium temperature, stating that densification proceeds by grain boundary sliding controlled by serial interface/reaction steps involving diffusion of Zr^{4+} and/or Y^{3+} into the lattice. Several investigations carried out on 3Y-ZrO_2 and 8Y-ZrO_2 mention the requirement of a post- SPS thermal treatment to recover white ceramic sample, in particular when sintering is conducted at a temperature higher than 1050°C [10, 11]. While some authors attribute the grey/black color to carbon contamination (graphite environment of SPS) [14, 15], others, in the absence of XRD evidence in particular, consider that the color change during SPS could be the consequence of oxygen non-stoichiometry [10, 11]. However, the occurence of oxygen vacancies resulting from SPS was not specifically investigated.

By varying the experimental conditions, this study aims to investigate oxygen vacancies created during SPS and their potential role on both densification and tetragonal phase stabilization. The targeted SPS temperature window is below 900°C, which has been found highly sensitive in terms of both densification and color changes. Indeed, we have already proved that the combination of Cold Sintering Process (CSP) and SPS is a highly effective approach to obtain dense ceramics at temperatures as low as 850°C [16]. So, in a first part, this report focuses on the combined CSP-SPS approach showing the influence of the sintering environment on densification. In the second part, we will demonstrate that the vacuum conditions in the SPS chamber is a key parameter to improve densification in a single SPS step of the 3Y-ZrO_2 ceramics at such low temperature. A combination of characterizations targeting the

presence of oxygen vacancies is proposed. The role of point defects in SPS densification of yttria stabilized zirconia is discussed.

2. Experimental

Commercial 3Y-ZrO_2 nanopowder (US Research Nanomaterials, 20 nm) was used. In section 3.1, samples were prepared by a combined approach involving a first step by CSP (91°C, 440 MPa, 150 min) followed by a second step by SPS (850°C, 100 MPa, 90 min, under argon). The CSP temperature was set in the dehydration temperature window of the zirconium carbonate, precisely determined by thermal analysis performed in our previous work [16]. Experiments were performed with a Syntex model Dr Sinter Lab. 515-S SPS machine using graphite dies, spacers and punches. These sintering conditions were applied to four samples: 3Y-ZrO_2 with and without the addition of 3 wt.% $(ZrO_2)_2CO_2.xH_2O$. The samples were isolated from the die and punches using either graphite foil or Inconel 625 foil and discs in order to avoid any contact with carbon. In section 3.2, yttria zirconia powder without any additive has been directly sintered by SPS at 850°C and 100 MPa, during 20 min at constant pressure and temperature. The heating ramp was set at 50°C/min until 850°C. The cooling rate was set to 30°C/min down to room temperature. A post-heating treatment required to eliminate carbon contamination was set at 750°C during 2 hours with a heating and cooling ramp of 1°C/min. In section 3.2, three different pressure levels in the SPS chamber were tested: i) after evacuating until a base pressure down to 10^3 Pa, the chamber is refilled with Argon up to reach static atmospheric pressure, ii) a dynamic primary vacuum of 10 Pa iii) enhanced vacuum of 2.10^{-2} Pa achieved by dynamic pumping using two devices, a primary vacuum pump combined with an oil diffusion pump. For these experiments, a 5-minute pre-cycle at 500°C is used to minimize the quantity of adsorbed species within the chamber and carbon elements, thus facilitating pressure decrease. In addition, this pre-cycle avoids desorption during the temperature rise, which helps maintaining a pressure of 2.10^{-2} Pa during sintering. In this case, a Penning gauge (cold cathode ionization gauge) enables precise pressure measurement during the densification process.

The relative density of the ceramic after SPS was evaluated by geometric measurements and Archimedes method in ethanol.

X-ray diffraction patterns were performed at room temperature on both powder and ceramics using a PANalytical X'Pert MDP Bragg-Brentano diffractometer equipped with a secondary monochromator. The Cu $K_{\alpha1}$, $K_{\alpha2}$ radiations are generated at 40kV and 40mA. The phase proportions (tetragonal/monoclinic) of the ceramics have been determined from room temperature X-ray diffraction patterns using the methodology developed by R.C. Garvie *et al.* and Toraya *et al.* [17, 18]. It consists in measuring the integrated areas of three peaks: (11-1) et (111) corresponding to the monoclinic phase (28.2° et 31.2° (2θ), respectively) and (111) corresponding to the tetragonal phase (30.3° (2θ)).

High Resolution Scanning Electron Microscopy (HRSEM) analysis of the fracture surfaces of the samples was carried out on SEM-JEOL-6700 equipment at the PLACAMAT platform (University of

Bordeaux, France). To optimize charge evacuation during analysis, samples are metallized by PVD deposition of a 1.5 nm-thick layer of platinum.

Thermogravimetric analyses data of the materials were recorded under an N_2/O_2 (80%/20%) flow between 30 and 900 °C. The experiments were performed on a thermogravimeter NETZSCH STA 449 F5 Jupiter coupled with QMS 403 D Aeolos Quadro simultaneous analyzer (Netzsch, Germany). Before the characterization the whole system was purged 30 min under Argon atmosphere and filled with N_2/O_2 during 10 min. About 10 or 20 mg of the sample was placed in a crucible and heated up to 900°C at a heating rate of 5°C/min. The evolved gas was transported to the mass spectrometer through a transfer line at 200°C and continuously analyzed during the experiment. The ion current was detected from the gaseous molecules as m/z 2 and 60. To characterize the release of CO_2 the ion current of m/z =44 was recorded related to the temperature.

A ThermoFisher Scientific K-ALPHA spectrometer was used for X-ray Photoelectron Spectroscopy (XPS) surface analysis with a monochromatized AlKα source (hν=1486.6 eV) and a 400 microns X-Ray spot size. Prior to characterization, the powders were pressed onto indium foil and the pellets were fractured. The sample holder was directly placed into vacuum and transferred into the analysis chamber when the pressure reached 10^{-5} Pa. The full spectra (0-1150 eV) were acquired with a constant pass energy of 200 eV and high-resolution spectra with a constant pass energy of 40 eV. Charge neutralization was applied during analysis. Slight sputtering was performed with low energy Ar^+ ions (i.e. 480s sputtering corresponding to about 60 nm in depth). High resolution spectra (i.e. C1s, O1s, Zr3d, Y3d) were quantified (Scofield sensitivity factors applied) and fitted using the AVANTAGE software provided by ThermoFisher Scientific. Concerning O1s, a model with 3 Lorentzian/Gaussian components of similar Full Width at Half Maximum (FWHM) was applied.

Electron Paramagnetic Resonance (EPR) experiments were performed using a Bruker ESP300E X-band spectrometer equipped with an Oxford Instruments ESR900 He-flow cryostat. The EPR spectra were recorded at room temperature (293 K) and low temperature (30 K) using the following parameters: microwave frequency 9.54 GHz, microwave power 50 mW, magnetic field modulation frequency and amplitude 100 kHz and 0.3 or 0.8 mT, respectively, conversion time 82 ms and spectral resolution 0.1 or 0.5 mT/pt. DPPH (g = 2.0036) was used as external reference.

The emission spectra were obtained using a Edinburg FLS1000 spectrofluorometer equipped with a PM R980 detector. A 450W continuous Xe lamp was used as the excitation source. All the measurements were performed at room temperature. The luminescence spectra were corrected for the sensitivity of the detectors and response of grating (1200 lines).

Electrochemical Impedance Spectroscopy (EIS) measurements were performed using a Frequency Response Analyzer AUTOLAB PGSTAT302. A two contacts sample holder was used with gold grids as current collectors. The set-up allows performing measurements from 25 °C to 900 °C under controlled gas (air, nitrogen, argon). The frequency range extends from 1 Hz - 1 MHz. The dimensions of the studied samples were around 10 mm in diameter and 2 mm in thickness. Highly homogeneous platinum

of electrodes of 300 nm thickness were deposited on both sample surfaces by Plasma Vapour Deposition. Measurements were then carried out at 50°C intervals in the temperature range from 200 to 800°C. Data were modelled using ZView® software program to determine the electrical characteristics using equivalent circuits.

3. Results and discussion

3.1. Combined CSP-SPS process: creation of oxygen vacancies and associated defects

We have already proven that the combination of two processes, CSP and SPS, is an effective route to trigger densification of tetragonal 3Y-ZrO_2 up to 92-95% below 900°C [16]. In particular, we demonstrated that the key point relies in a transient chemical reactivity induced during the Cold Sintering Process (CSP). The successive steps of dehydration and destabilization of an amorphous hydrated zirconium carbonate triggers a specific chemistry tuned *in-situ* during the thermal cycle. While the central role of chemistry in sintering mechanisms and transport pathways has been clearly highlighted, the identification of the defects involved has not been fully addressed, in particular during the SPS. To do so, the influence of the sintering environment during SPS on both the densification and the post-annealing steps was first probed. As described in the experimental part, samples were prepared starting from 3Y-ZrO_2 commercial nanopowder with and without the addition of 3 wt.% $(ZrO_2)_2CO_2.xH_2O$. CSP compacts were densified in a second step by SPS using either graphite or Inconel 625 protective foils and discs, all other experimental conditions being identical. Table 1 shows the relative densities of the samples determined by Archimedes' method, and the tetragonal/monoclinic phase ratios assessed from the X-ray patterns.

Table 1: Relative densities and weight fractions of tetragonal and monoclinic phases obtained for the samples elaborated by combining CSP (91°C, 440 MPa, 150 min) and SPS (850°C, 100 MPa, 90 min, under argon). C refers to graphite tools, I to Inconel and A to the addition of zirconium carbonate.

Sample name	***Initial powder***	***Sample environment during SPS***	***Relative density (%)***	***$Y_{monoclinic}$ (wt.%)***	***$Y_{tetragonal}$ (wt.%)***
3Y- ZrO_2-C	3Y- ZrO_2	Carbon	89.5	2	98
3Y- ZrO_2-CA	3Y-ZrO_2 + 3 wt.% $(ZrO_2)_2CO_2.xH_2O$	Carbon	95	5	95
3Y- ZrO_2-I	3Y-ZrO_2	Inconel 625	89.3	0	100
3Y- ZrO_2-IA	3Y-ZrO_2 + 3 wt.% $(ZrO_2)_2CO_2.xH_2O$	Inconel 625	92	3	97

Relative densities in the range 89-95% were obtained for all the ceramics prepared using the combined CSP - SPS approach. The tetragonal phase was stabilized at a weight ratio larger than 95%, and even more without the reactive agent $(ZrO_2)_2CO_2.xH_2O$. This is consistent considering the crystallization of monoclinic ZrO_2 grains from the decomposition of the carbonate at T > 600°C [16]. As reported in this previous work, using hydrated zirconium carbonate allows to reach high densities (> 92%) [16]. Moreover, these densities were reached whatever the nature of the protecting foils (graphite or Inconel). It should be noted that for all conditions, a color change towards blue/grey was observed for all ceramics after SPS, pointing towards charged defects. In order to specifically target the role of the environment during SPS, thermal and XPS characterizations were first carried out on ceramics produced without additives. Thermal analyses performed immediately after SPS, showed the absence of CO_2 desorption in between 20°C and 900°C when Inconel 625 foils were used (Fig. 1 b). This observation was supported by XPS investigation of the sample conducted before any post-annealing that confirms the absence of carbon contamination as well as any metal contamination from Inconel foils (Fig. 2 c, d). Indeed, all the indexed lines can be assigned to Zr, Y, O atoms whether the spectrum was recorded from the extreme surface of the ceramic or after etching. The sample was nevertheless blue color, which might suggest the presence of oxygen vacancies. In the case of SPS ceramics performed with a graphite environment, thermal analysis shows that carbon species were eliminated in the temperature range 700 to 750°C (Fig.1 a). This shows that thermal analysis coupled with mass spectrometry is a relevant tool for accurately assessing the post-SPS heat treatment conditions required to eliminate carbon contamination during sintering. This post-thermal annealing is very often required after the SPS sintering step for many functional oxides, and its impact on chemistry, microstructure and stress relaxation is not neutral. It is therefore important to accurately target the annealing conditions, and not to impose excessively high temperatures or excessively long annealing times. This methodology could therefore be applied to the optimization of thermal cycles for a wide range of materials densified by SPS.

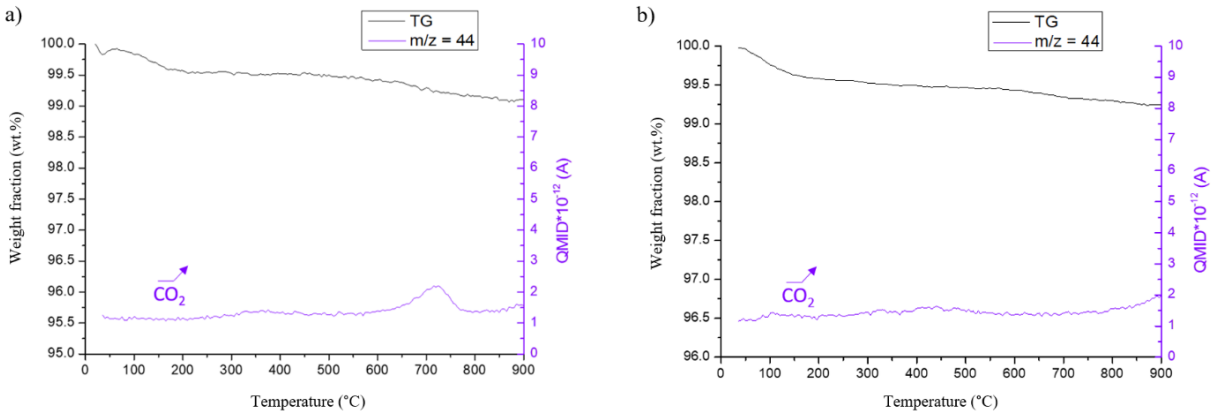

Figure 1: TGA and associated quadrupole mass spectra showing CO_2 desorption of (a) 3Y- ZrO_2-C and (b) 3Y- ZrO_2-I samples before annealing at 750°C for 2 hours. The ion current of m/z =44 was recorded to follow the desorption of CO_2.

As expected, XPS analysis performed on sample sintered in graphite environment exhibits a significant amount of carbon even after etching (see Fig. 2 a). Large sample contamination (~80% carbon) can be noticed. Despite being etched for 150 seconds, the amount of carbon remains constant, demonstrating that carbon is not only present at the extreme surface but also deeper in the ceramic. As shown by the thermal analyses (Fig. 1), the 2 hours post heat treatment in air at 750°C (R = 10°C/ min) was effective in eliminating all carbonaceous species (Fig. 2 b).

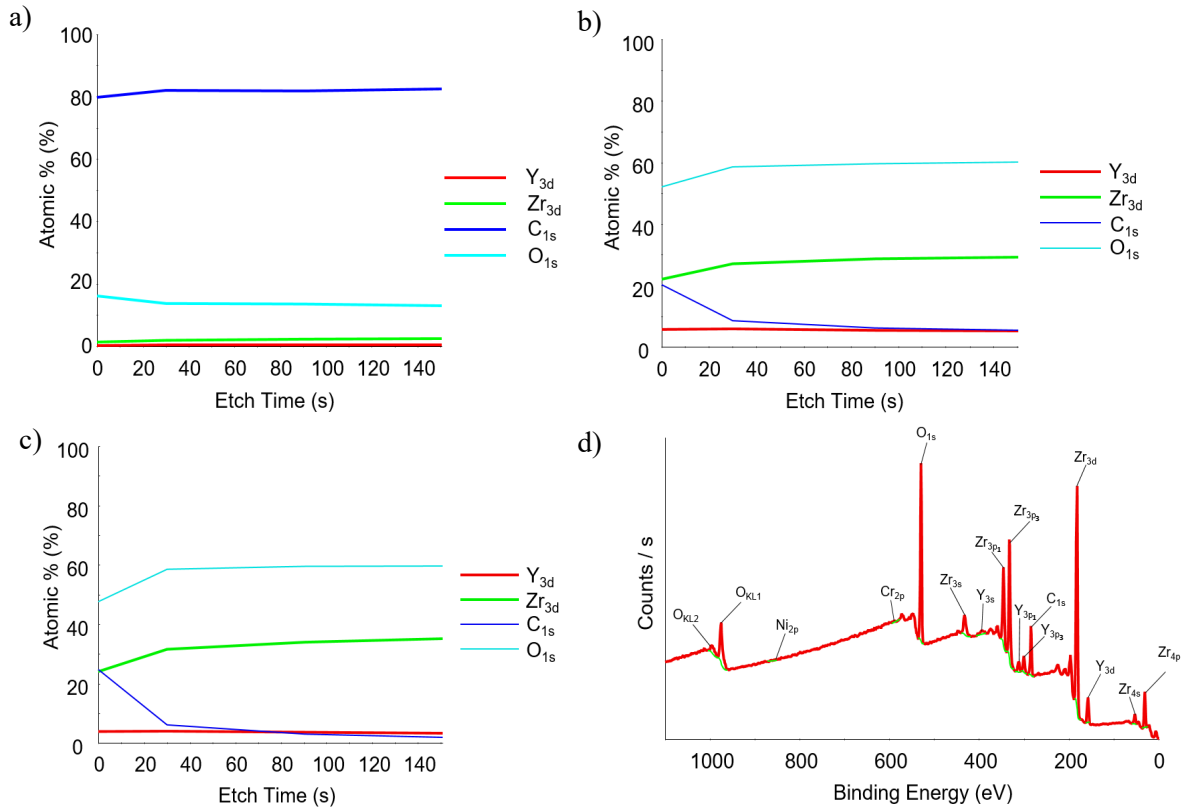

Figure 2: Atomic profiles on surfaces of the samples (a) 3Y-ZrO_2-C before annealing, (b) 3Y- ZrO_2-C after annealing at 750°C during 2 hours and (c) 3Y-ZrO_2-I before annealing. (d) XPS survey spectrum of 3Y-ZrO_2-I before annealing at 750°C. Argon etching was carried out at a stripping speed = 0.37 $nm.s^{-1}$. The residual surface carbon in b), c) and d) is a standard contamination during the transfer to the XPS chamber.

Figure 3 shows that the O1s XPS spectrum of a 3Y- ZrO_2 sample processed by CSP-SPS with a carbon environment can be deconvoluted by two major contributions, centred at 529.6 eV and 531.5 eV. While some studies ascribe the 531-532 eV signal in the XPS spectrum of O1s to oxygen vacancies (the 530 eV signal corresponding to O^{2-} in the crystal lattice), surface carbonation and/or hydroxylation also induce signals in this energy range: O-H and C=O at around 531.5 eV and O-C at around 532.5 eV. (Fig. 3 a) [19-21]. In addition, while it was expected that the post-SPS heat treatment restores oxygen stoichiometry in the material, there was no significant difference between the O1s signals of the sample before (Fig. 3 a) and after post SPS annealing (Fig. 3 b). As a result, considering the likely hydroxylation and surface carbonation in ambient air of the samples characterized in our study, no conclusion regarding the creation of vacancies during CSP-SPS sintering can be drawn from the O1s spectra.

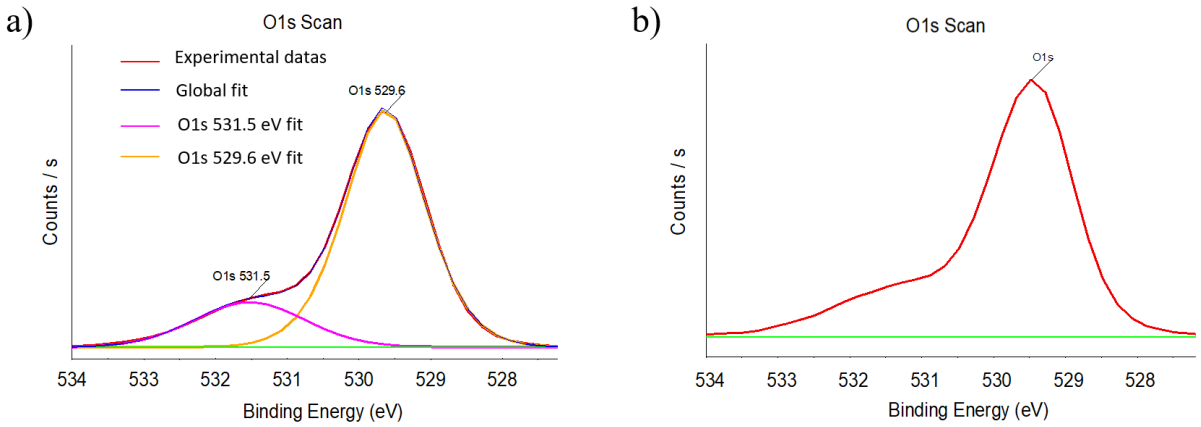

Figure 3: XPS O1s spectra corresponding to 3Y-ZrO_2-C by CSP-SPS at 850°C (a) before and (b) after post-SPS heat treatment at 750°C during 2h.

Targeting point defects and their relation to the densification, Electron Paramagnetic Resonance investigation were performed to better understand the gain in relative density obtained when 3Y-ZrO_2 is sintered with the addition of the hydrated zirconium carbonate (either using graphite or Inconel foils and discs). For reference, the initial 3Y-ZrO_2 commercial nanopowder was also probed.

EPR analyses of the two CSP-SPS crushed ceramics and not air annealed post SPS, showed two main resonance signals in the magnetic field range from 300 to 380 mT (Figs. 4 b-c). First, an axial signal with two components $g_{\perp}$ = 1.975 and $g_{//}$ = 1.959 was detected, which was already identified in the literature as corresponding to paramagnetic Zr^{3+} species [22, 23]. This type of defect involves an oxygen vacancy in the direct vicinity of Zr^{4+} cations with an extra electron located in its 4d orbital and not trapped in the anionic vacancy, hence leading to the formation of Zr^{3+} cations. A second signal, isotropic, sharp and intense, was observed at a g value of 2.0027, close to that associated with delocalized free electrons in the conduction band (g = 2.0023) [24]. However, as already mentioned, carbon radicals on

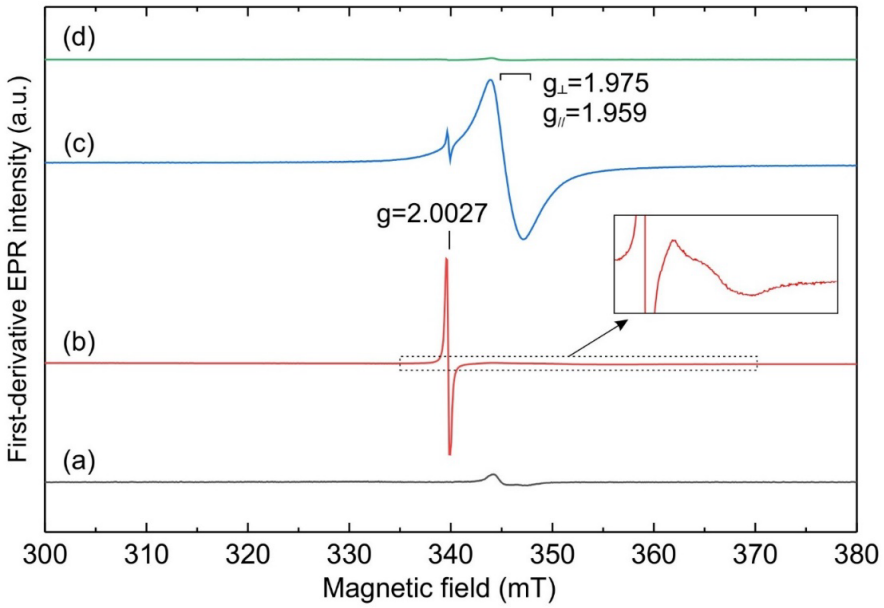

Figure 4: X-band EPR powder spectra recorded at 30K for a) the initial 3Y-ZrO_2 powder, (b) 3Y-ZrO_2-CA (c) 3Y-ZrO_2-IA (d) 3Y-ZrO_2-CA after post thermal treatment at 750°C during 2h.

the surface must be taken into account because their EPR signal is centred on values of g ~ 2.00. Indeed, this signal is particularly intense for the sample processed under carbon environment, but it is also detected for an Inconel 625 environment (Fig. 4 c). Since no Carbon was detected in XPS (excepted on extreme surface) (Fig. 2c), the isotropic signal at g = 2.0027 could correspond to the presence of electrons trapped in oxygen vacancies, i.e. F^+ centers (a single electron associated with a vacancy: VO^+). The shape of the signal is due to the spherical symmetry of the wave function corresponding to the F^+ centers, resulting from an isotropic electron environment [24-26].

The value of g, very close to that of free electrons, and the symmetry of the signal indicate a certain mobility of electrons in the vacancy lattice. In addition, the potential presence of diamagnetic F centers (two trapped electrons) within CSP-SPS ceramics, which are not detectable by EPR, cannot be overlooked. The presence of these F and F^+ centers, inducing absorption bands in the visible wavelengths, may explain the blue/gray color of CSP-SPS-densified ceramics.

Figure 4 a shows a low-intensity signal at $g_{\perp}$ = 1.975 and $g_{//}$ = 1.959, indicating that the starting powder already contains Zr^{3+} species that may arise from the nanopowders synthesis, which generates surface defects and oxygen substoichiometry when the nanoparticle size is within the range of 20 nm. In addition, TiO_2 impurities, present in low concentrations (around 55 ppm) in the starting powder, must be mentioned as the Ti^{3+} species gives EPR signals at $g_{\perp}$ = 1.97 and $g_{//}$ = 1.99, which are very close to Zr^{3+} [27]. Nevertheless, the very high signal intensities at $g_{\perp}$ = 1.975 and $g_{//}$ = 1.959 of the samples processed by CSP-SPS (Figs. 4 b-c) cannot be due solely to the presence of Ti^{3+}. Furthermore, the strong difference in signal intensity corresponding to Zr^{3+} species between samples densified with Inconel 625 (Fig. 4 c) and graphite (Fig. 4 b) shows that this signal does not originate from an impurity. The observed differences in intensity concern the two main signals (at g = 2.0027, $g_{\perp}$ = 1.975 and $g_{//}$ = 1.959 in Figs. 4 b-c), demonstrating a clear influence of the sintering environment in the distribution of defects within the material. In the case of all graphite SPS tools, the signal identified as corresponding to F^+ centers located in the volume and/or at grain boundaries was very intense compared with the signal attributed to Zr^{3+} species. On the contrary, the most intense signal corresponds to the one attributed to Zr^{3+} species at $g_{\perp}$ = 1.975 and $g_{//}$ = 1.959 in the case of the sample processed with the Inconel 625 foils. It should be noted here that after the 2-hour post-SPS heat treatment at 750°C in air, the signal corrsponding to the color center became very weak. Reoxydation of the material was effective and a white color was recovered.

At room temperature (293 K), the EPR spectrum of the sample processed in the carbon environment (Fig. 5-(b)) exhibits an additional resonance line (peak-to-peak linewidth ~70 mT) centered at about 325 mT (g = 2.1). As the temperature decreases down to 30 K, this signal shifts towards low fields, becomes broader and its peak-to-peak intensity decreases significantly, indicating the possible presence of clusters of Zr^{3+} species and/or F^+ centers involved in ferromagnetic-type couplings. The intensity and the temperature dependence of this ferromagnetic resonance line is much less marked for the sample densified with the Inconel 625 foils, suggesting more isolated paramagnetic species. Note that the signal

observed at 150 mT for all samples corresponds to the presence of Fe^{3+} impurities (39 ppm Fe_2O_3 in the starting powder).

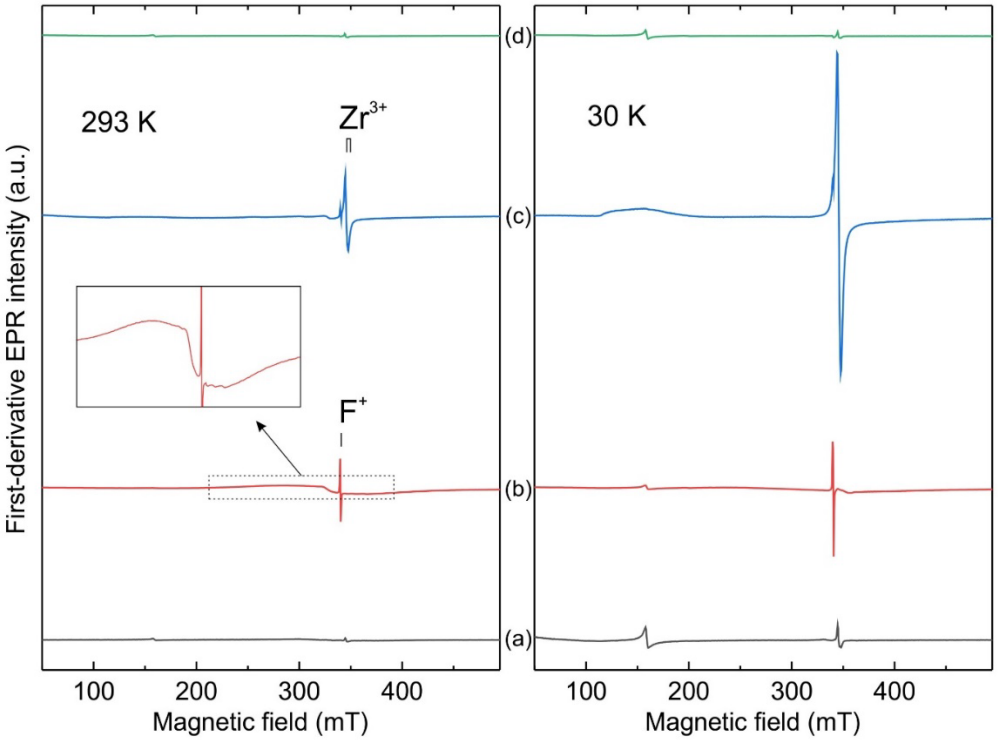

Figure 5: X-band EPR spectra at 293K and 30K performed on a) the initial 3Y-ZrO powder, (b) 3Y-ZrO_2-CA (c) 3Y-ZrO_2-IA (d) 3Y-ZrO_2-CA after post thermal treatment at 750°C during 2h.

Finally, in order to probe the influence of the addition of the reactive agent during the two-step process, EPR spectra were performed on the ceramic obtained using Inconel foils with and without $(ZrO_2)_2CO_2.xH_2O$ (SI Fig. 1). The EPR spectra of the two samples showed the presence of paramagnetic Zr^{3+} species, whose distribution within the ceramics significantly differs. A single, relatively broad signal was detected for the sample without addition of the reactive agent, which is characteristic of the presence of clusters of Zr^{3+} species (SI Fig. 1 a). In the case of the sample 3Y-ZrO_2 + 3 wt.% $(ZrO_2)_2CO_2.xH_2O$, the axial signal at $g_L = 1.975$ and $g_{//} = 1.959$ was finer, well defined and more intense (Fig. 1SI-b). A higher concentration of isolated Zr^{3+} species may therefore be proposed. On the other hand, the fine, isotropic signal at g = 2.0027 was only detected for the ceramic 3Y-ZrO_2 + 3 wt.% $(ZrO_2)_2CO_2.xH_2O$. This result raises again the question of the assignment of the signal at g=2.0027, it cannot be ruled out that this signal arises from the presence of carbon radicals resulting from the decomposition of zirconium carbonate during the SPS step. Nevertheless, considering the large difference in intensity of this signal observed in Figures 4 b-c, for a similar amount of hydrated zirconium carbonate added to the initial powder mixture, the hypothesis of the presence of F^+ centers remains more consistent (particularly in view of the signal symmetry) and in agreement with the literature [24, 26].

All the EPR characterizations revealed the formation of F^+ centers and Zr^{3+} species associated with the creation of oxygen vacancies during the densification of 3Y-ZrO_2 using the combined CSP-SPS approach with or without the addition of a hydrated zirconium carbonate. The creation of points defects was clearly shown when using this approach, and can be related to the high level of densification reached at temperature as low as 850°C. The use of Inconel was shown to be highly effective in preventing carbon contamination and enabling more accurate identification of the present paramagnetic species. The link between color and creation of defects was here clearly established. The different samples tested show that the environment during the SPS step (graphite, Inconel, reactive agent) did not modify the nature of the point defects created. In contrast, the environment significantly impacted their density and distribution. In a graphite environment, a majority of F^+ centers were observed in volume or localized at grain boundaries compared to Zr^{3+} sites, as well as the presence of local clusters of paramagnetic species interacting by ferromagnetic coupling (Fig. 5). The sample processed with the Inconel 625 foils showed predominantly Zr^{3+} species at the expense of F^+ centers, with a very homogeneous distribution of these Zr^{3+} sites. In addition, EPR analyses displayed a different paramagnetic species signature for ceramics made by CSP-SPS with and without the addition of hydrated zirconium carbonate (Inconel foils), in terms of distribution of defects in particular. The ceramic made of 3Y-ZrO_2 + 3 wt.% $(ZrO_2)_2CO_2.xH_2O$ presented a more homogeneous distribution of Zr^{3+} paramagnetic species and possibly a higher concentration of these isolated species associated with oxygen vacancies. The configuration and position of vacancies in the lattice is rather complex and depend mainly on two factors, the electrostatic interactions and the differences in ionic radii due to substitution Zr^{4+}/Y^{3+} [28]. A higher density of oxygen vacancies leads to the clustering of defects, occurring along predefined crystallographic directions (depending on Y^{3+} concentration) in order to balance electrostatic and deformation energy (steric effect) [28]. Isolated and well distributed oxygen vacancies do not favor vacancy-vacancy interactions or ordering of vacancies, that would reduce the mobility of oxygen [29]. The correlation between the spatial distribution of point defects and the rate of densification cannot be clearly established here. However, the presence of Zr^{3+} confirms the formation and stabilization of oxygen vacancies after SPS and raises the question of their contribution to the densification mechanism. Even if the commonly accepted mechanism is the cationic diffusion (Zr^{4+} being the slowest species), the indirect role of the oxygen vacancies on the cationic mobility should be considered. It can be pointed out that in the temperature range between 800 and 900°C, the density of the ceramics was found to be very sensitive to the different experimental parameters (temperature/applied pressure couple, addition of a reactive agent). Thus, even if the combined CSP-SPS approach promoted a high-level densification at low temperature (850°C), the reproducibility remained limited as shown by the variability in density values ranging between 85 and 95% according to the experiments. Different parameters could explain this variability, such as the application of high pressures at low temperature during the CSP (stacking defects, cracks), high sensitivity of the hydrated zirconium carbonate, multi-stage process. However, our results highlight a common feature associated with both activation of densification and stabilization

of tetragonal phase at low temperature, the contribution of oxygen vacancies. The next part is thus dedicated to the investigation of the densification of 3Y-ZrO_2 in one step by SPS at 850°C, exploring different level of oxygen partial pressure in the SPS chamber.

3.2 Monitoring the oxygen partial pressure during SPS: impact on densification, structural and microstructural features

In this section, the objectives will be to demonstrate if the vacuum level in the SPS chamber has a significant impact on densification and tetragonal phase stabilization through the formation of oxygen vacancies in early stage of sintering at low temperature. For these experiments, graphite foils and discs around the samples have been used. The SPS sintering cycle was set as follows: a temperature of 850°C, a pressure of 100 MPa applied at room temperature and a dwell time of 20 min. Three different levels of vacuum were used as described in the experimental section, 10^3, 10 and 2.10^{-2} Pa. Whatever the vacuum conditions, all samples were blue/gray after sintering, with a more pronounced color when the oxygen partial pressure during sintering was low. After the post-SPS heat treatment in air at 750°C, all the ceramics recovered a white color.

The relative density of the samples increased systematically when the level of vacuum within the SPS chamber was lowered, reaching values higher than 96% (Fig. 6). The stabilization of the tetragonal phase followed the same trend, even if the values remain high and in a narrow range (from about 95 to 99 wt.% tetragonal) (Fig.7b). Considering experimental conditions with a vacuum level of 2.10^{-2} Pa, a relative density between 96.7 and 98.8% and a stabilization of the tetragonal phase as high as 99 wt.% were obtained (Fig. 6).

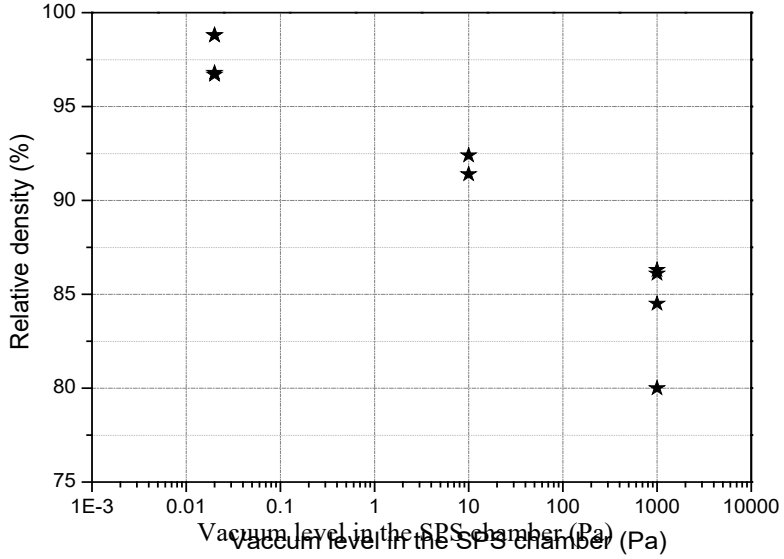

Figure 6**:** Relative densities of SPS-processed 3Y-ZrO_2 samples (850°C, 100 MPa, 20 min) at different vacuum levels within the SPS chamber. Different experiments were conducted for each vacuum level.

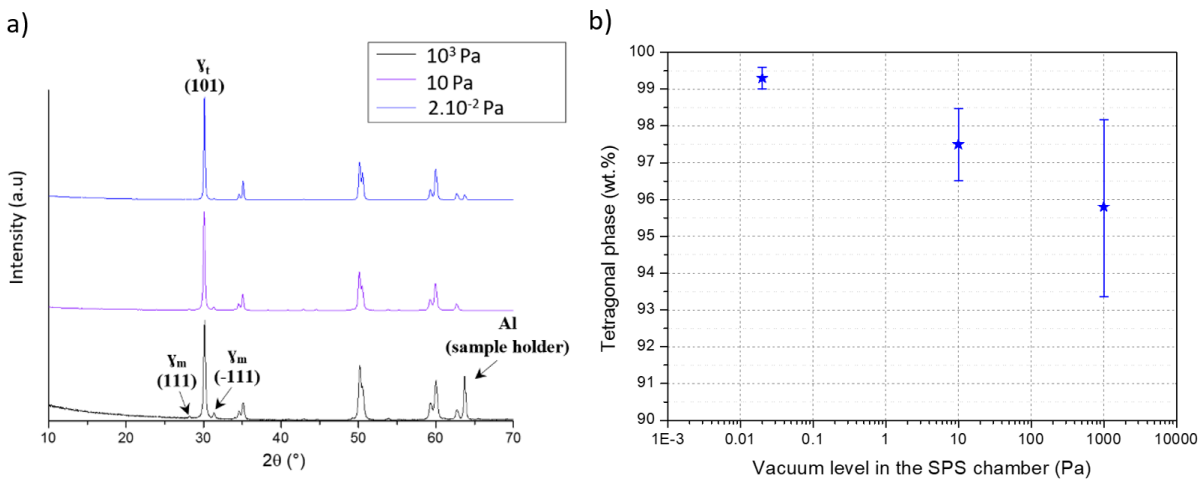

Figure 7: a) XRD patterns of the SPS-processed 3Y-ZrO_2 samples (850°C, 100 MPa, 20 min) at different vacuum levels within the SPS chamber. The peak at 2θ = 64° corresponds to the aluminium sample holder. b) Evolution of the tetragonal mass fraction according to the vacuum level in the SPS chamber.

As the tetragonal phase is stabilized by a mechanism of charge compensation and oxygen vacancy formation, maintaining the oxygen sub-stoichiometry in the crystal lattice can lead to further stabilization of the tetragonal phase, by decreasing the oxygen density around the Zr^{4+} cations. The dominant role of oxygen vacancies and their distribution within the cationic lattice on the stabilization of the tetragonal phase was clearly demonstrated by Fabris *et al.* [5]. In addition, the blue/gray color of the ceramics after sintering attests from the presence of color centers, a single electron associated with a vacancy: VO^+ (as shown in section 3.1). It is worth noting a high reproducibility of the experiments: the three samples performed at 2.10^{-2} Pa present respective relative densities of 96.7%, 98.8% and 98.8% (Fig. 6). Using an initial chamber pressure level of 10^3 Pa, the density drops and the reproducibility is lost (Fig. 6). This last result shows that the main reason for the lack of reproducibility of the results in section 3.1 relies not necessarily on the two-step process but on a poor control of the oxygen partial pressure within the chamber at the beginning of the sintering. Figure 8 shows the evolution of SPS chamber pressure during the thermal cycle. Two samples were selected for vacuum levels at 10 Pa (blue and black curves) and 2.10^{-2} Pa (orange and pink curves). In both cases, pressure control by dynamic pumping ensures that the target pressure was maintained throughout the process. As the temperature of the system increases, outgassing was observed, but the pressure stabilizes at the target pressure level during the first few minutes of the temperature plateau. These outgassings can be assigned to the desorption of species from the 3Y-ZrO_2 starting powder and from the SPS chamber and graphite elements.

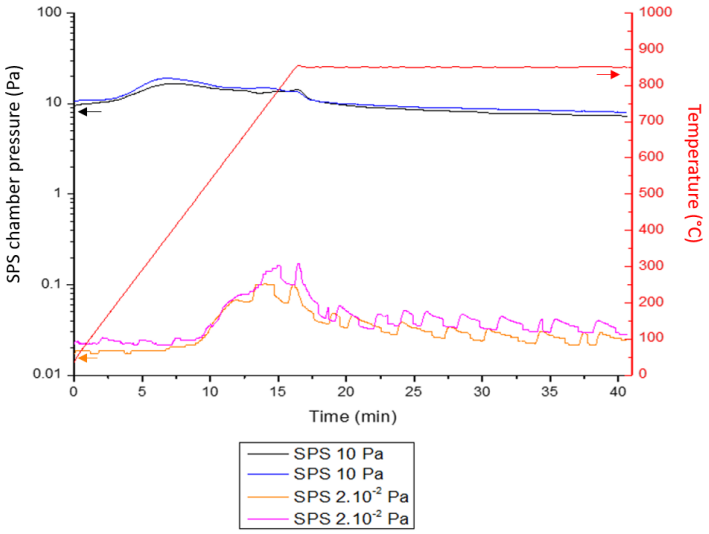

Figure 8**:** Evolution of the SPS chamber pressure during the sintering cycle for samples elaborated at 10 Pa and 2.10^{-2} Pa. Note that the instabilities observed for conditions of 2.10^{-2} Pa (orange and pink curves) result from desorption during the temperature rise and the high precision of the measurement allowing to detect very small outgassing.

Dilatometric monitoring of the samples was carried out throughout the process (Fig. 9). While the distance between the two electrodes of the SPS device can be measured over time, it is nevertheless necessary to substract from the measurements the contribution of all elements external to the sample. These experiments were all carried out in a mold and with spacers that had already undergone an initial temperature rise to 850°C, in order to consider, the thermal expansion of these elements. In agreement with the relative densities determined by Archimedes' method (mentioned on Fig. 6), the lower the oxygen partial pressure in the chamber, the greater the final shrinkage. Thus, a final vertical shrinkage of 2 to 2.1 mm was measured for samples densified at a vacuum level of 2.10^{-2} Pa (two samples were tested to ensure reproducibility), compared with 1.2 mm for the sample processed at 10^3 Pa, whose final relative density was only 80% (Fig. 9). While the general profile of the vertical shrinkage curves over

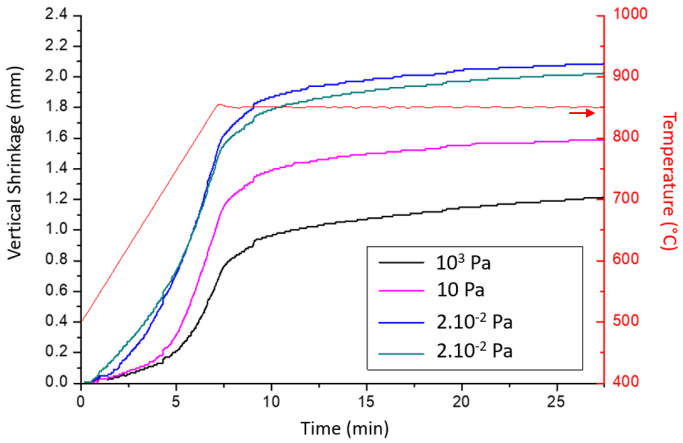

Figure 9: Vertical shrinkage curves of samples during SPS densification at 850°C, 100 MPa, 20 minutes. The red curve shows the temperature of the samples over time.

the entire sintering cycle follows a quasi-similar trajectory for all four samples, the oxygen partial pressure in the chamber seems to play a key role in the early stages of densification as the system heats up. Indeed, lowering the oxygen partial pressure induces a shift in the onset of densification towards lower temperatures.

Various hypotheses can be put forward concerning the effect of vacuum level on densification activation during temperature rise. Firstly, a higher vacuum promotes the removal of impurities and adsorbed species present in the starting powder. The "cleaned" surface powder is then more reactive, which lowers the temperature at which sintering necks are formed. On the other hand, it can be argued that defect formation is favoured at lower temperatures under high-vacuum conditions. The formation of oxygen vacancies could promote the initiation of surface diffusion phenomena and play a role in the formation of necks at an earlier stage. A beneficial effect of a low oxygen partial pressure atmosphere on the initiation of densification in the early stages of sintering has been reported by Levi *et al.* in the case of $BaTiO_3$ sintering by SPS [30].

HRSEM micrographs of the fractures of densified samples in the three different environments (Fig. 10) confirmed the significant variation in relative density as a function of oxygen partial pressure in the chamber during sintering. Consequent microstructural changes were observed with regard to densification advancement, grain faceting and grain growth. Under the sintering conditions used, a vacuum level corresponding to a low oxygen partial pressure (2.10^{-2} Pa) induced an advanced stage of densification (faceted grains, low porosity) while limiting grain growth (Figs. 10 c-c').

A mixed intergranular/intragranular fracture pattern was observed. An average grain size of 64.3 ± 3.0 nm was determined over measurements on 250 particles. However, a broader grain size distribution was observed compared to the two other ceramics, with a large proportion of grains retaining a moderate size ranging from 40 to 50 nm (similar to that observed for lower densification rates), and some grains reaching sizes ranging from 100 to 200 nm. A mechanism of coalescence of small grains into larger ones at the final stage of sintering can be put forward and linked to a mechanism of grain growth by displacement of grain boundaries, as proposed in the work that Flaureau *et al.* carried out on an identical initial powder [13]. Grain growth by coalescence via nanograin sliding and rotation has also been reported in nanocrystalline YAG and Y_2O_3 powders sintered by SPS [31, 32]. Further investigations are required to identify the governing factors for different grain growth mechanisms. For samples densified with a vacuum level of 10^3 in the SPS chamber (Figs. 10 a-a'), the presence of open porosities has been observed, while morphology and grain size remain very close to those of the starting powder. These observations were in good agreement with the relative density measurements reported on these samples. Finally, micrographs shown on figures 10 b-b' are well representative of an intermediate stage of densification associated with a lower porosity rate than for the sample processed at a vacuum level of 2.10^{-2} Pa and a slightly more pronounced faceted grain morphology.

Regarding the identification of possible defects, characterization by EPR of the samples processed by SPS at 850°C and 100 MPa for 20 minutes and under different vacuum conditions (not having undergone

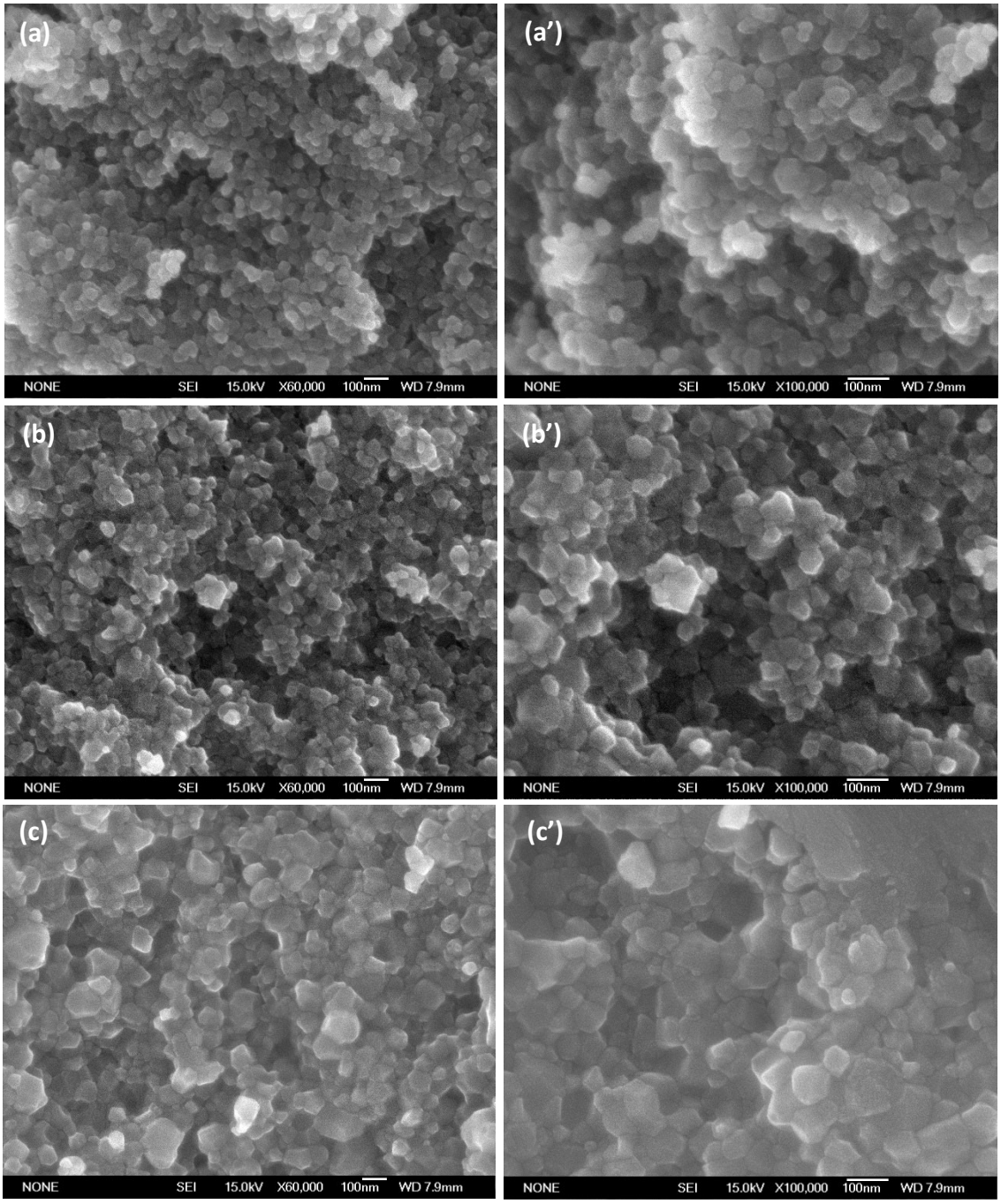

Figure 10: HRSEM images of the fracture surfaces of the 3Y-ZrO_2 ceramics processed by SPS (850°C, 100 MPa, 20 min) at different vacuum level within the SPS chamber. (a) et (a') 10^3 Pa, (b) et (b') 10 Pa, (c) et (c') 2.10^{-2} Pa.

post-heat treatment in air) did not show any significant evolution of the signal corresponding to paramagnetic Zr^{3+} species (g_L = 1.975 and $g_{//}$ = 1.959) as a function of oxygen partial pressure during densification (not shown). Moreover, the recorded signal at g_L = 1.975 and $g_{//}$ = 1.959 was very weak in comparison with the EPR study presented in section 3.1 on ceramics obtained by the combined CSP and SPS approach. At this stage, the EPR characterizations do not allow any conclusions to be drawn about the point defects generated during SPS sintering of 3Y- ZrO_2 at low oxygen partial pressure.

Given the coloration of the ceramics obtained, a photoluminescence spectroscopy study was carried out. Blue luminescence was observed in the two samples tested (10^3 Pa and 2.10^{-2} Pa), which were not

reoxidized in air post SPS, but crushed by hand in a mortar for these characterizations. For an excitation wavelength of λ = 230 nm, both samples show a broad emission band with a symmetrical shape (Fig. 11 b) between 300 and 600 nm. This emission was not detected on the 3Y-ZrO_2 starting powder. The spurious emissions observed between 300 and 380 nm (Fig. 11 a) are due to the fluorescence of one of the spectrometer components and will not be discussed in the present article.

According to figure 11, the emission band observed can be correlated to the presence of oxygen vacancies within the ceramics. Ultraviolet irradiation of the compound creates an electron-hole pair. The electron delocalized in the conduction band is then trapped on an oxygen vacancy, leading to the

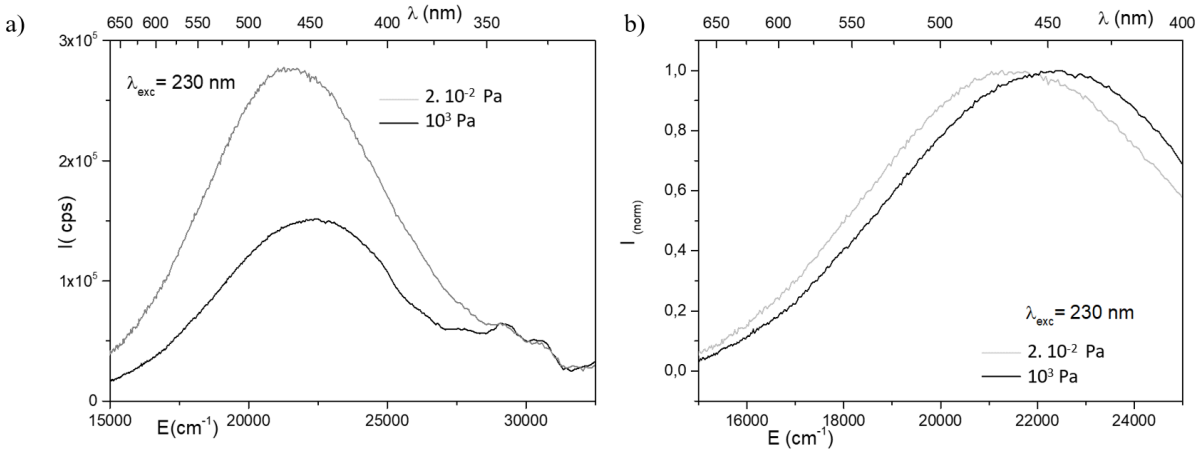

Figure 11: Emission spectra of ceramics obtained at 850°C, 100 MPa, 20 minutes for vacuum levels corresponding to 2.10^{-2} Pa and 10^3 Pa, for an excitation wavelength of 230 nm: a) with spurious emission normalized at the maximum value and (b) with emission centred at 450 nm normalized (normalization to the maximum of emission).

stabilization of a F-color center [33, 34]. This observation echoes the analyses made by EPR previously. The radiative de-excitation associated with the recombination of the electron with the hole left in the valence band gives rise to visible emission. The initial stabilization of oxygen vacancies could explain the blue/gray color of 3Y-ZrO_2 ceramics produced by SPS. As far as visible emission is concerned, the role of additional impurities in the initial powder cannot be overlooked. Indeed, various studies report an increase in radiative emissions between 400 and 600 nm resulting from the introduction of trivalent ions such as Ti^{3+} [35]. The luminescence observed is not, however, associated with the E_g-T_{2g} transitions of trivalent titanium. On the other hand, the transition metal would play a non-negligible role in the proportion of stabilized oxygen vacancies, the creation of F centers under irradiation and the recombination of electron-hole pairs [33]. While the presence of Ti^{3+} was not detected in the EPR and XPS analyses carried out on the probed samples, it is not possible to totally rule out its contribution due the presence of TiO_2 impurities in the initial powder (55 ppm TiO_2 according to the manufacturer). Normalizing peak intensity with respect to spurious emission (Fig. 11 a), the higher intensity of the emission band in the case of a vacuum level of 2.10^{-2} Pa, could indicate a greater proportion of color centers than for the sample processed at 10^3 Pa. However, this difference in intensity may also be due to light reflection/diffusion phenomena depending on powder particle size. For accurate quantification, controlled sample grinding and a powder sieving step would be necessary. It is highly likely that the

emissions in the visible range are due to the stabilization of oxygen vacancies. Even if at this stage the specific origin of the point defects cannot be formally established, and a significant difference as a function of vacuum conditions has not been clearly demonstrated, these results are consistent with EPR analyses.

In order to better understand the microstructural properties of the ceramics, electrochemical impedance spectroscopy measurements have been performed. Indeed, the electrochemical response of a material to the application of an alternating current is intimately dependent on its structural, microstructural and chemical characteristics [36-38]. In the case of yttria stabilized zirconia, a solid electrolyte, conductivity is linked to the migration of O^{2-} anions via oxygen vacancies. Several studies have focused on impedance spectroscopy characterization of yttria stabilized zirconia ceramics (in particular 8Y-ZrO_2) obtained by various sintering processes [39-42]. Hence, the electrical behaviour of SPS ceramics elaborated using

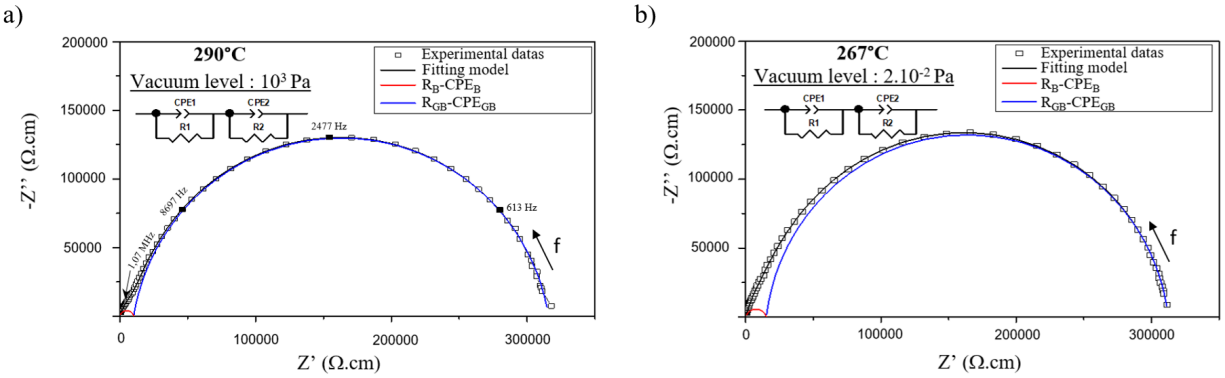

Figure 12: Nyquist representations of two samples processed by SPS at 850°C and 100 MPa for 20 min with different vacuum levels in the SPS chamber (a) 10^3 Pa and (b) 2.10^{-2} Pa. These measurements were carried out under nitrogen flow before the samples were heat-treated in air at 800°C.

different levels of vacuum (10^3 Pa and 2.10^{-2} Pa), before and after post-SPS heat treatment in air, which is assumed to restore oxygen stoichiometry, have been explored. The objective being to examine a potential change in ionic transport properties due to the formation of oxygen vacancies resulting from the specific SPS conditions selected. The data were collected under steady state conditions, on heating between 200 and 800°C under a nitrogen flow to avoid any reoxidation of the ceramics. Then, at the beginning of a dwell of 2h at 800°C, an air flow was introduced and the same impedance measurements were done at the same temperatures on cooling under air. The Nyquist diagrams show two contributions (frequencies centered around 20 kHz and 1 to 2 MHz - Fig. 12). The contribution at lower frequencies appears to dominate whatever the sintering conditions in terms of vacuum level (Figs. 12 a-b). The EIS data were fitted with a two-contribution model: one intragranular (Bulk) and the other intergranular (grain boundaries) located at high and low frequencies, respectively. These two contributions are then modelled by an equivalent circuit composed of two R// CPE blocks in parallel (called R-CPE) associated in series where a resistor and a Constant Phase Element are associated in parallel (Fig. 12).

In the case of the two SPS samples studied (vacuum level: 2.10^{-2} Pa and 10^3 Pa), the two contributions have a very close equivalent capacitance of the order of around 2.10^{-10} F.cm-1 (Fig. 13). For sake of

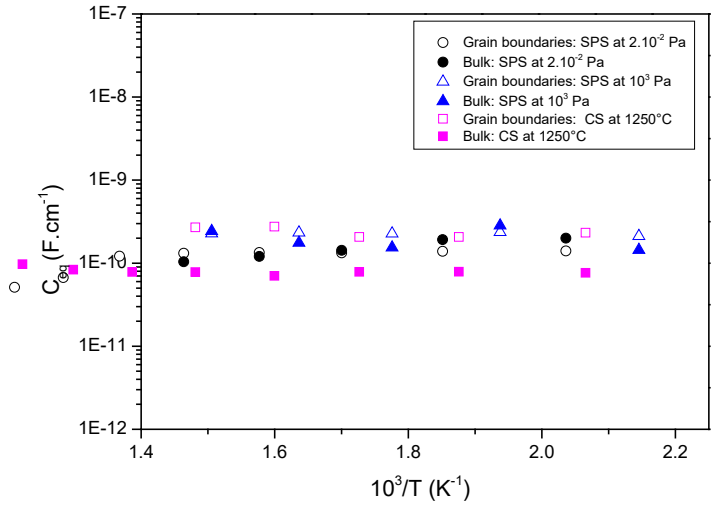

Figure 13: Thermal behavior of the equivalent capacitance determined from impedance measurements on samples processed by SPS at two pressure levels in the SPS chamber and comparison with a sample processed by conventional sintering at 1250°C during 2 hours (CS 1250°C).

comparison, a dense ceramic (d_{rel} ~ 98,5%, made with the same starting powder) was produced by conventional sintering at 1250°C with dwell time of 2h (heating ramp of 2°C/min). Almost similar values and equivalent capacitance trends were observed (Fig.13). However, for the conventional ceramic (average grain size 159 ± 43 nm), the Ceq values of the two resistive contributions slightly differ, Ceq_{GB} ~ 2.10^{-10} F.cm^{-1} (Grain Boundaries) and Ceq_B ~ 8.10^{-11} F.cm^{-1} (Bulk). This difference is smaller compared to the values reported in the literature, e.g. Ceq_{GB} ~ 4.10^{-10} F.cm^{-1} and Ceq_B ~ 8.10^{-11} F.cm^{-1} for 3Y-ZrO_2 ceramics produced by SPS at 1200°C (grain size > 200nm) [41]. This difference could be explained by a microstructural effect. Considering the Brick Layer Model [43-46] and based on the relationship $\frac{\delta_{GB}}{G} = \frac{C_G}{C_{GB}}$ (where δ_{GB} and G are the grain boundary thickness and average grain size, respectively, and C_G and C_{GB} the grain and grain boundary capacitances) [37], a decrease in grain size (the values of δ_{GB} assumed to be equivalent) would result in closer equivalent capacitance values. This is indeed what we observed by EIS for the two SPS ceramics with grain sizes well below 100 nm (Fig. 10). The "over-representation" of the intergranular contribution at low frequencies (Fig. 12) can be explained by the high density of grain boundaries (average grain size of these ceramics between 40 and 70 nm) and by the non-negligible porosity rate of 15% in the case of the sample corresponding to a vacuum level of 10^3 Pa in SPS chamber, leading to a very high resistive contribution. It can therefore be established that the ionic transport mechanism is controlled by a very dominant contribution from grain boundaries (located at the lowest frequencies).

In the case of the sample processed at 2.10^{-2} Pa, the intragranular conductivity is significantly higher before than after heat treatment in air at 800°C (Fig. 14 b). This behavior is not observed for the sample densified at 10^3 Pa, for which almost equivalent intragranular conductivities are observed before and after heat treatment in air (Fig. 14 a). These results then support the hypothesis that the use of a high

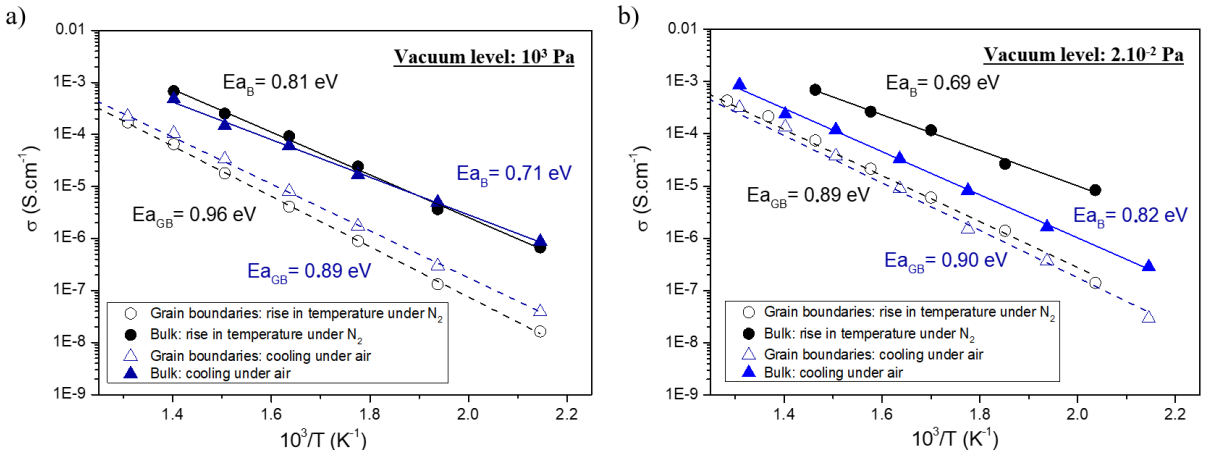

Figure 14: Conductivities before and after heat treatment in air at 800°C on samples processed by SPS at two vacuum levels a) 10^3 Pa and b) 2.10^{-2} Pa.

vacuum level during SPS sintering of 3Y-ZrO_2 at 850°C, can generate the formation of anionic vacancies in sufficient quantity to induce a significant increase in intragranular ionic mobility. It is interesting to note that this phenomenon is not observed on the transport properties of grain boundaries, implying that vacancies would be formed in volume rather than on the grain surface. It can therefore be deduced that heat treatment in air leads to partial or even total reoxidation of the ceramic (restoration of the initial oxygen stoichiometry) and hence a reduction in intragranular ionic conductivity (Fig. 14 b). Furthermore, the conductivity values obtained agree with those reported for 3Y-ZrO_2 ceramics produced by SPS at 1200°C [41], by conventional sintering [37, 42] or by flash sintering [41, 42].

Considering the relation $\sigma = \sigma_0 \, e^{-\frac{E_a}{RT}}$, the activation energy can be deduced from the thermal evolution of the conductivity. The activation energy associated with intragranular ionic migration for the sample obtained at 2.10^{-2} Pa (Ea_B = 0.69 eV, Fig. 14 b) is relatively low compared with that of 3Y-ZrO_2 ceramics densified by SPS and Flash SPS (0.86 eV) [41] or by conventional sintering at 1350°C and Flash sintering (0.95 eV) [42]. This demonstrates the influence of sintering conditions on anionic mobility. A change in stability and defect distribution can be induced by the specific conditions of low oxygen partial pressure. At the end of the heat treatment in air, ceramic reoxidation appears to be effective, given the white color and the increase in activation energy (Ea_B = 0.82 eV (Fig. 14 b)), confirming the hypothesis of oxygen vacancy formation during densification at low oxygen partial pressure. With regard to grain boundaries, the activation energies are consistent to those reported in literature [41, 42] and the post heat treatment under air does not lead to significant change.

The results of the electrochemical characterizations show the influence of oxygen partial pressure during SPS densification on the transport properties of the ceramics. These analyses are in line with those carried out by EPR and photoluminescence to study the nature of defects generated during SPS sintering. All these studies point to the formation of oxygen vacancies during densification of 3Y-ZrO_2 by SPS (850°C, 100 MPa, 20 min), with a higher concentration and/or mobility of oxygen vacancies under specific high-vacuum conditions (2.10^{-2} Pa). The various characterizations carried out by EIS also show

the effectiveness of post-SPS heat treatment on ceramic reoxidation. With regard to the differences in equivalent capacitances and conductivities as a function of sintering conditions and during post-SPS annealing, the influence of microstructural characteristics correlates well with the evolution of grain size, grain boundary density and porosity rate).

Focusing on densification, it can be noted that an electric field promoted nucleation of oxygen vacancies at the grain boundaries was highlighted in Flash Sintering [42]. As a consequence, and compared to conventional sintering, enhanced densification was observed. However, as shown by the equivalent activation energies whatever the sintering process, the flash sintering-induced modification of the defect profile at the grain boundaries does not lead to significant change in the electrical transport mechanism governed by oxygen vacancies [42]. In the present study and in view of all the characterizations, the formation of oxygen vacancies under SPS conditions is unambiguous. The distribution of the oxygen vacancies and, above all, the temperature window at which they are formed are influenced by SPS conditions. The very small particle size (<100nm) and the presence of defects contribute to very high surface reactivity, which at low temperatures exalts the surface diffusion and possibly grain rotation/sliding mechanisms responsible for the onset of granular growth.

4. Conclusion

This study focused on 3Y-ZrO_2 ceramics, explored the potential of the SPS process for optimizing yttria stabilized zirconia densification at temperatures as low as 850°C. Two approaches were considered, one based on a combination of CSP-SPS processes, the other on a single SPS step. The set of experimental conditions tested and the analysis of results enabled correlations to be established between SPS experimental parameters, defect formation and the activation of densification at low temperatures. In particular, the control of the vacuum level in the SPS chamber was identified as a critical parameter with a significant influence on densification in a restricted temperature range below 900°C. By lowering the vacuum level in the SPS chamber to 2.10^{-2} Pa, densification rates up to 98.8% were achieved at 850°C (100 MPa and 20 min dwell time). Under these specific conditions, this remarkable increase in density is associated with very low grain growth (<100nm) and high stabilization of the tetragonal phase (>98%). Analysis of the defects generated during sintering was investigated using specific and complementary characterization techniques. A first result is based on the identification by EPR of the formation of oxygen vacancies and Zr^{3+} species, whose distribution depends on the CSP-SPS conditions. Characterization of the SPS ceramics by photoluminescence and electrochemical impedance spectroscopy showed that low oxygen partial pressure in the SPS chamber leads to a higher concentration of oxygen vacancies during sintering. These conditions favour an exaltation of nanoparticle surface reactivity via defect formation in the early stages of sintering, with activation of surface diffusion leading to the formation of sintering necks at lower temperatures. The creation of oxygen vacancies could then play an indirect role in facilitating cationic diffusion (increasing the number of surface defects and modifying the chemical environment of Zr^{3+} and Zr^{4+} cations in the

vicinity of oxygen vacancies). The temperature at which these point defects are generated is lowered at low oxygen partial pressure. Defect chemistry and its role in the densification of yttria stabilized zirconia at low temperatures remains particularly complex to understand and requires further study. The most striking and original result is the identification of the SPS chamber vacuum level as the decisive experimental parameter for zirconia densification at 850°C. The particularly high-density values obtained for moderate experimental conditions, including in terms of applied pressure, attest to the relevance of this strategy.

5. Acknowledgments

6. References

[1] R. Garvie, J. Hannink, R. Pascoe., Ceramic steel?, Nature 258 (1975) 703-704.

[2] M. Yoshimura, Phase stability of Zirconia, Ceramic Bulletin 67 (1988) 1950-1955.

[3] R. Garvie, The occurrence of metastable tetragonal zirconia as a crystallite size effect, J. Phys. Chem. 69 (1965) 1238.

[4] M.W. Pitcher, S.V. Ushakov, A. Navrotsky, B.F. Woodfield, G. Li, J. Boerio-Goates, B.M. Tissue, Energy crossovers in nanocrystalline zirconia, J. Am. Ceram. Soc. 88 (2005) 160–167.

[5] S. Fabris, A.T. Paxton, M.W. Finnis, A stabilization mechanism of zirconia based on oxygen vacancies only, Acta Materialia 50 (2002) 5171–5178.

[6] M. Raza, D. Cornil, J. Cornil, S. Lucas, R. Snyders, S. Konstantinidis, Oxygen vacancy stabilized zirconia (OVSZ): a joint experimental and theoretical study, Scripta Materialia 124 (2016) 26-29**.**

[7] John W. Drazin, Ricardo H.R. Castro, Phase Stability in Nanocrystals: A Predictive Diagram for Yttria–Zirconia, J. Am. Ceram Soc. 99 (2016)1377-1384

[8] P. Li, I. W. Chen, and J. E. Penner-Hahn, Effect of Dopants on Zirconia Stabilization - an X-Ray Absorption Study: II, Tetravalent Dopants, J. Am. Ceram. Soc. 77 [5] (1994)1281–8.

[9] J. Chevalier, L. Gremillard, A. V. Virkar, D. R. Clarke J. Am. Ceram. Soc., 92 [9] (2009)1901–1920.

[10] U. Anselmi-Tamburini, J.E. Garay, and Z.A. Munir, A. Tacca and F. Maglia, G. Chiodelli, G. Spinolo, Spark plasma sintering and characterization of bulk nanostructured fully stabilized zirconia: Part II. Characterization studies, J. Mater Res 19 (2004) 3263.

[11] G. Bernard- Granger and Christian Guizard, Spark plasma sintering of a commercially available granulated zirconia powder: I. Sintering path and hypotheses about the mechanism(s) controlling densification, Acta Materialia 55 (2007) 3493-3504.

[12] J. Langer, M. J. Hoffmann,y and O. Guillon. Electric Field-Assisted Sintering in Comparison with the Hot Pressing of Yttria-Stabilized Zirconia, J. Am. Ceram. Soc. 94 (2011) 24-31.

[13] A. Flaureau, A. Weibel, G. Chevallier and C. Estournès, Study of the densification and grain growth mechanisms occurring during spark plasma sintering of different submicronic yttria-stabilized zirconia powders, J. of the Eur. Ceram. Soc. 41 (2021) 3581-3594.

[14] T. Takeuchi, I. Kondoh, N. Tamari, N. Balakrishnan, K. Nomura, H. Kageyama and Y. Takedab, Improvement of Mechanical Strength of 8 mol % Yttria-Stabilized Zirconia Ceramics by Spark-Plasma Sintering, J. Electrochem. Soc. 149 (2002) A455 -A461.

[15] X.J Chen, K.A Khor, S.H Chan and L.G Yu Preparation yttria-stabilized zirconia electrolyte by spark-plasma sintering, Mater. Sci. Eng. A 341[1,2] (2003) 43-48.

[16] M.I. Rua Taborda, E. Martin, U.C. Chung, S. Fourcade, C. Labrugère, D. Michau, G. Goglio, C. Elissalde, A new chemical pathway towards densification of tetragonal zirconia below 900 °C Materialia 24 (2022) 101479.

[17] R.C. Garvie, P.S. Nicholson, Phase Analysis in Zirconia Systems, J. Am. Ceram. Soc 55[6] (1972) 303-5.

[18] H. Toraya, M. Yoshimaru, Calibration Curve of Quantitative Analysis of the Monoclinic-Tetragonal ZrO_2 System by X-Ray Diffraction, J. Am. Ceram. Soc. 67[6] (1984) C119-21.

[19] Y. Zeng, Z. Lai, Y. Han, H. Zhang, S. Xie and X. Lu, Oxygen-Vacancy and Surface Modulation of Ultrathin Nickel Cobaltite Nanosheets as a High-Energy Cathode for Advanced Zn-Ion Batteries. Adv. Mater. 30 (2018)1802396.

[20] Z. Wang, X. Mao, P. Chen, M. Xiao, S. A. Monny, S. Wang, M. Konarova, A. Du, L. Wang, Understanding the Role of Oxygen Vacancies in Hematite-Based Photoelectrochemical Processes, Angew. Chem. Int. Ed. 58 (2019) 1030–1034.

[21**]** H. Idriss, On the wrong assignment of the XPS O1s signal at 531–532 eV attributed to oxygen vacancies in photo- and electro-catalysts for water splitting and other materials applications, Surface Science 712 (2021)121894.

[22] A. F. Bedilo, M. A. Plotnikov, N. V. Mezentseva, A. M. Volodin, G. M. Zhidomirov, I. M. Rybkin and K. J. Klabunde, Superoxide radical anions on the surface of zirconia and sulfated zirconia: formation mechanisms, properties and structure. *Phys. Chem. Chem. Phys.* 7 (2005) 3059-69

[23] C. Morterra, E. Giamello, L. Orio and M.Volante, Formation and reactivity of zirconium(3+) centers at the surface of vacuum-activated monoclinic zirconia, J. Phys. Chem. 94 (1990) 3111–3116.

[24] C. Gionco, M. Paganini, E. Giamello, R. Burgess, C. Valentin and G. Pacchion, Paramagnetic Defects in Polycrystalline Zirconia: An EPR and DFT Study, Chem. Mater. 25 (2013) 2243–2253.

[25] C. B. Azzoni, A. Paleari and F. Scardina, Electron Trapping Sites Near Oxygen Vacancies in Stabilized Zirconia, Sensors and Materials 8[4] (1996) 217-221.

[26] R. Ben-Michael, D. S. Tannhauser, and J. Genossar, ESR centers in reduced stabilized zirconia, Phys Rev B, 43[10] (1991) 7395-7404.

[27] P. Lombard, N. Ollier and B. Boizot, EPR study of Ti^{3+} ions formed under beta irradiation in silicate glasses, Journal of Non-Crystalline Solids 357 (2011) 1685–1689.

[28] A. Navrotsky, Thermochemical insights into refractory ceramic materials based on oxides with large tetravalent cations, J. Mater. Chem. 15 (2005)1883-1890.

[29] D. Marrocchelli, P. A. Madden, S. T. Norberg and S. Hull, Structural Disorder in Doped Zirconias, Part II: Vacancy Ordering Effects and the Conductivity Maximum, Chem. Mater. 23 (2011) 1365–1373.

[30] R. D. Levi and Y. Tsur, The Effect of Oxygen Vacancies in the Early Stages of $BaTiO_3$ nanopowder Sintering, Adv. Mater. 17 (2005)1606–1608.

[31] R. Chaim, Grain coalescence by grain rotation in nano-ceramics, Scripta Materialia, 66 (2012) 269-271.

[32] R. Marder, R. Chaim and C. Estournès, Grain growth stagnation in fully dense nanocrystalline Y_2O_3 by spark plasma sintering, Mater. Sci. Eng. A527 (2010) 1577-1585.

[33] Y. Cong, B. Li, S. Yue, D. Fan, and X. Wang, Effect of Oxygen Vacancy on Phase Transition and Photoluminescence Properties of Nanocrystalline Zirconia Synthesized by the One-Pot Reaction, J. Phys. Chem. C 113 (2009)13974–13978.

[34] S. V. Nikiforov, A. A. Menshenina and S. F. Konef, The influence of intrinsic and imputity defects on the luminescent properties of Zirconia, Journal of Luminescence, 174 (2016) 49-55.

[35] J. M. Carvalho, L.C.V. Rodrigues, J. Hölsä, M. Lastusaari, L.A.O. Nunes, M. C.F. Felinto, O.L. Malta and H.F. Brito, Influence of titanium and lutetium on the persistent luminescence of ZrO_2, Opt. Mater. Express 2[3] (2012) 331-340.

[36] M. Filal, C. Petot, M. Mokchah, C. Chateau and J. L. CarpentierIonic conductivity of yttrium-doped zirconia and the "composite effect", Solid State Ionics 80 (1995) 27–35.

[37] M. C. Steil, F. Thevenot and M. Kleitz, Densification of Yttria-Stabilized Zirconia Impedance Spectroscopy Analysis, J. Electrochem. Soc. 144[1] (1997) 390-398.

[38] X. J. Chen, K. A. Khor, S. H. Chan and L. G. Yu, Influence of microstructure on the ionic conductivity of yttria-stabilized zirconia electrolyte, Materials Science and Engineering: A 335 (2002) 246–252.

[39] U. Anselmi-Tamburini, J. E. Garay and Z. A. Munir, Spark plasma sintering and characterization of bulk nanostructured fully stabilized zirconia: Part II. Characterization studies, J. Mater. Res. 19[11] (2004) 3263-3269.

[40] J. Langer, M. J. Hoffmann and O. Guillon, Electric Field-Assisted Sintering in Comparison with the Hot Pressing of Yttria-Stabilized Zirconia, J. Am. Ceram. Soc. 94 [1] (2011) 24–31.

[41] T. Hérisson de Beauvoir, Z. Ghomari, G. Chevallier, A. Flaureau, A. Weibel, C. Elissalde, F. Mauvy, R. Chaim, C. Estournès, Flash Spark Plasma Sintering of 3YSZ: Modified sintering pathway and impact on grain boundary formation, J. Eur. Ceram. Soc. 41[15] (2021) 7762-7770.

[42] J. C. M'Peko, J.-C., Francis, J. S. C. & Raj, R. Impedance Spectroscopy and Dielectric Properties of Flash Versus Conventionally Sintered Yttria-Doped Zirconia Electroceramics Viewed at the Microstructural Level. J. Am. Ceram. Soc. 96 (2013) 3760–3767.

[43] X. Guo, Size dependent grain-boundary conductivity in doped zirconia, Computational Materials Science 20 (2001) 168-176.

[44] H. L. Tuller, Ionic conduction in nanocrystalline materials, Solid State Ionics 131 (2000) 143 -157.

[45] J.C.C. Abrantes, J.A. Labrincha and J.R. Frade, Applicability of the brick layer model to describe the grain boundary properties of strontium titanate ceramics, J. Eur. Ceram. Soc. 20 [10] (2000) 1603-1609.

[46] N. J. Kidner, N. H. Perry, T. O. Mason and E. J. Garboczi, The Brick Layer Model Revisited: Introducing the Nano-Grain Composite Model, J. Am. Ceram. Soc., 91 [6] (2008) 1733–1746.